

NUMERICAL STUDY OF NON-REACTING AND REACTING FLOW CHARACTERISTICS IN A LEAN DIRECT INJECTION COMBUSTOR

Dipanjay Dewanji

PhD Researcher

Faculty of Aerospace Engineering
Delft University of Technology
Netherlands

Arvind G. Rao

Assistant Professor

Faculty of Aerospace Engineering
Delft University of Technology
Netherlands

Mathieu Pourquie

Professor

Faculty of Mechanical Engineering
Delft University of Technology
Netherlands

Jos P. van Buijtenen

Professor

Faculty of Aerospace Engineering
Delft University of Technology
Netherlands

email: J.P.vanBuijtenen@tudelft.nl

ABSTRACT

The Lean Direct Injection (LDI) combustion concept has been of active interest due to its potential for low emissions under a wide range of operational conditions. This might allow the LDI concept to become the next generation gas-turbine combustion scheme for aviation engines. Nevertheless, the underlying unsteady phenomena, which are responsible for low emissions, have not been widely investigated. This paper reports a numerical study on the characteristics of the non-reacting and reacting flow field in a single-element LDI combustor. The solution for the non-reacting flow captures the essential aerodynamic flow characteristics of the LDI combustor, such as the reverse flow regions and the complex swirling flow structures inside the swirlers and in the neighborhood of the combustion chamber inlet, with reasonable accuracy. A spray model is introduced to simulate the reacting flow field. The reaction of the spray greatly influences the gas-phase velocity distribution. The heat release effect due to combustion results in a significantly stronger and compact reverse flow zone as compared to that of the non-reacting case. The inflow spray is specified by the Kelvin-Helmholtz breakup model, which is implemented in the Reynolds-Averaged Navier

Stokes (RANS) code. The results show a strong influence of the high swirling flow field on liquid droplet breakup and flow mixing process, which in turn could explain the low-emission behavior of the LDI combustion concept.

1 Introduction

The future environmental regulations and the economical issues are the main driving forces behind the development of modern gas-turbines with essential features like low pollutant emissions and high efficiency. For aircraft gas-turbines, the vision set for the year 2020 and beyond imposes additional challenges to the development of gas-turbine design to meet the requirements of lowering harmful emissions and specific fuel consumption. It is a well known fact that increasing pressure ratios and turbine inlet temperatures improve the thrust level and the engine cycle efficiency. Nevertheless, emissions of NO_x will increase with increasing pressure ratios and turbine entry temperatures, which will eventually jeopardize the low pollutant characteristics of gas-turbines [1].

Although major changes in the future engine designs are

most likely, combustion process will continue to influence the engine emission characteristics. Therefore, a great deal of attention has been focused on identifying innovative combustion approaches that could improve both engine cycle efficiency and emission levels. To achieve a low level of NO_x emissions, reducing the combustion flame temperature and the flow residence time are the two most effective and popular approaches. One recently investigated method that could incorporate both the NO_x abatement techniques into one design philosophy, is the Multi-point Lean Direct Injection (MPLDI) methodology [2, 3]. As shown in Figure 1, a set of small swirler-injectors are employed to attain a uniform combustion caused by the direct fuel injection into the combustor. Fuel and air are injected at an equivalence ratio close to the Lean Blowout (LBO) limit, which essentially reduces the combustion zone temperature. The arrangement of the multi-burning zones will cause strong interactions among themselves, thereby expediting the fuel-air mixing process. As a result, a complete combustion can be achieved within a short combustor length. Furthermore, since the amount of air required for combustion is injected directly, no dilution regions are required, leading to a more compact combustor with less structural weight.

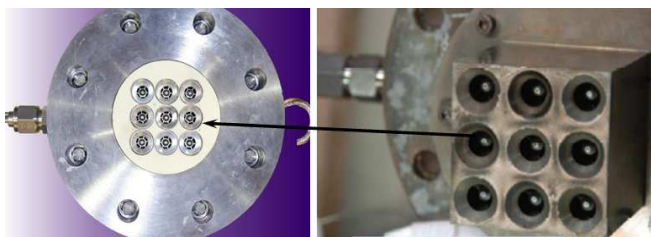


Figure 1. The Multi-Point LDI (MPLDI) combustor geometry

Nevertheless, before investigating the complex MPLDI combustor, it is important to understand how each small swirler behaves in an actual combustion environment. Therefore, in this paper, as a first step, an effort is made to simulate a single-element LDI combustor. Simulations for both non-reacting and reacting flows are performed to compare with the measurement data [4]. Unsteady Reynolds Averaged Navier Stokes (URANS) code is used to simulate the non-reacting flow field. The realizable $\kappa - \epsilon$ and the Reynolds Stress Turbulence Model (RSTM) are used to specify the turbulence. For the reacting case, steady state RANS with the realizable $\kappa - \epsilon$ turbulence scheme is used to model the continuous phase, and the discrete phase model (DPM) with the unsteady particle tracking scheme is implemented to characterize the liquid fuel droplets. The liquid fuel droplets essentially represent the discrete phase. The continuous and the discrete phase are coupled in such a way that the discrete phase

trajectories are allowed to impact the gas-phase equations. However, the spray modeling offers challenges for the following reasons. The typical sprays consist of an initial dense regime where the liquid jet breaks up leading to significant particle-particle interactions. On the other hand, in the downstream, the droplet dispersion creates a dilute spray regime. Due to the reduced volumetric fraction of the liquid in the dilute regime, it may be preferred for modeling. But it is impossible to avoid the dense spray regime and the associated jet breakup process, which can possibly influence the subsequent dispersed spray. Unfortunately, both experiments and the available computational models could not give full resolution of the liquid jet breakup in the dense spray regime [5]. So there are many unsolved issues pertaining to the breakup process and its incorporation within the numerical models. There are two most popular breakup models, which can be implemented in RANS simulation, namely the Taylor Analogy Breakup (TAB) model [6] and the Kelvin-Helmholtz (K-H) model, have been widely used. In the present study, the latter model is used for its capability in resolving droplet breakup process induced by high weber-number flows. In addition to the K-H breakup model, the dynamic-drag model (DDM) is implemented to characterize the drag effects on drop's acceleration. Furthermore, turbulent dispersion of the droplets is defined by the Stochastic tracks model. The mixture-fraction/ beta PDF equilibrium chemistry model is used to predict the combustion of the vaporized fuel. The grid used for the computation is sufficiently refined until no appreciable changes are observed in the flow field.

The solution for the non-reacting flows in the single-element configuration captures the essential flow features of LDI combustor, such as the complex highly turbulent flow field inside the swirlers and in the combustion chamber and the reverse flow regions at the center of the injector, near the wall corners, and on the divergent section of the venturi. The components of the mean and turbulent velocities are studied at various axial locations inside the combustion chamber, which exhibit good agreement with the measurement data [4]. For the reacting case, a compact but stronger central recirculation zone is observed as compared to the recirculation zone seen in the non-reacting case. The paper also discusses about the temperature profiles and the trajectories of liquid droplets, which are not explained in the measurements. However, as a next step, efforts are currently underway to simulate the reacting flow field using URANS and LES, in order to explain the unsteady dynamics within the flow field. In addition, the droplet velocities, its size and distribution are under investigation.

The paper is structured as follows. In the next section, the mathematical formulation used in the present investigation are briefly discussed. In Section 3, the experimental setup and the numerical approach are summarized. This is followed by results and discussion in Section 4 and conclusions in Section 5.

2 Mathematical Formulation

The mathematical models that are used in the simulation are presented briefly in this section. The Fluent® code is used for the simulation, which implements the Euler-Lagrange approach to treat the multi-phase flow. The gas-phase is treated as continuum by solving the Navier-Stokes equations, while the dispersed phase is solved by tracking the liquid particles through the calculated flow field.

2.1 Gas-Phase equations

The governing equations for the gas phase include equations of mass, momentum, and energy conservation, supplemented by the turbulence model equations. The interactions between the spray drops and the gas phase is accounted for by considering the exchange functions.

In the absence of liquid drops, the gas-phase mass conservation equation is

$$\int_{Vol_g} \left\{ \frac{\partial \rho_g}{\partial t} + \nabla \cdot (\rho_g \mathbf{u}) \right\} dVol_g = 0 \quad (1)$$

where ρ_g is the gas density and \mathbf{u} is the velocity of the gas.

When the spray drops are present, the differential form of the gas-phase mass conservation equation becomes

$$\int_{Vol} \left\{ \frac{\partial \rho}{\partial t} + \nabla \cdot (\rho \mathbf{u}) \right\} dVol = - \int_{Surf_d} \rho_g (\mathbf{u} - \mathbf{w}) \cdot \mathbf{n}_d dA \quad (2)$$

where ρ is the gas mass per unit volume of the mixture, $Surf_d$ are the inner surfaces of the control volume in contact with the drops, \mathbf{w} refers to the interface velocity, and dA is an element of total surface area.

For an individual drop, the rate of change of liquid mass due to evaporation can be expressed as

$$\frac{\partial}{\partial t} \left(\frac{4}{3} \pi r^3 \rho_l \right) = \int_{Surf_d} \rho_l (\mathbf{w} - \mathbf{v}) \cdot \mathbf{n}_d dA \quad (3)$$

where ρ_l is the liquid density, \mathbf{v} is the drop velocity and the integration is over the surface of the drop. For mass conservation, the right hand sides of the Eqns 2 and 3 must be equal. When Eqn 3 is summed over all of the drops, and the liquid density is assumed to be constant, Eqn 2 becomes

$$\frac{\partial \rho}{\partial t} + \nabla \cdot (\rho \mathbf{u}) = \int \int \int \rho_l 4 \pi r^2 R f dr dv dT_d \quad (4)$$

This is the final form of the mass conservation equation, where R is time rate of change of drop radius, r , and T_d is the temperature of the drop.

Similarly, the momentum and energy equations can be obtained. For a single drop, linear momentum conservation gives

$$\frac{4}{3} \pi r^3 \rho_l \mathbf{F} = \int_{Surf_d} [\rho_g (\mathbf{u} - \mathbf{v})(\mathbf{v} - \mathbf{w}) \cdot \mathbf{n} - P_g \mathbf{n} + \boldsymbol{\tau}_g \cdot \mathbf{n} + \boldsymbol{\sigma} \nabla \cdot \mathbf{n}] dA \quad (5)$$

where \mathbf{F} is the acceleration of the drops, $\boldsymbol{\tau}_g$ is the viscous stress tensor of the gas, P_g is the thermodynamic pressure of the gas, and $\boldsymbol{\sigma}$ is the surface tension.

2.2 Spray equations and exchange terms

The spray equation [7] describes the evolution of the droplet distribution function, f , which has eleven independent variables. They include three droplet position coordinates \mathbf{x} , three velocity components \mathbf{v} , the drop radius coordinate r , the drop temperature T_d , the drop's distortion from sphericity y , the rate of change of drop distortion $dy/dt = \dot{y}$, and time t :

$$f(\mathbf{x}, \mathbf{v}, r, T_d, y, \dot{y}, t) dr d\mathbf{v} dT_d dy d\dot{y} \quad (6)$$

The above equation represents the probable number of droplets per unit volume. The time evolution of f is obtained by resolving a form of spray equation,

$$\begin{aligned} \frac{\partial f}{\partial t} + \nabla_{\mathbf{x}} \cdot (f \mathbf{v}) + \nabla_{\mathbf{v}} \cdot (f \mathbf{F}) + \frac{\partial}{\partial r} (f R) \\ + \frac{\partial}{\partial T_d} (f \dot{T}_d) \frac{\partial}{\partial y} (f \dot{y}) + \frac{\partial}{\partial \dot{y}} (f \ddot{y}) = \dot{f}_{coll} + \dot{f}_{bu} \end{aligned} \quad (7)$$

In the above equation, the terms \dot{f}_{coll} and \dot{f}_{bu} are the sources due to droplet collision and breakup respectively.

By solving the above spray equation and summing the rate of change of mass, momentum, and energy for all droplets at position \mathbf{x} and time t , the exchange functions between the continuous and discrete phase can be obtained. These exchange functions are the following:

1. the rate of mass evaporation from the droplets $\dot{\rho}^s$
2. the force transmitted to the gas through droplet drag, body forces and momentum exchange due to evaporation F^s
3. the energy transmitted to the gas by evaporation, heat transfer into the droplet, and work due to turbulent fluctuations \dot{Q}^s
4. the rate at which turbulent eddies do work in dispersing the droplets \dot{W}^s

These exchange functions determine the interactions between spray droplets and gas-phase flow field.

2.3 Atomization and Droplet Breakup Modeling

The pressure swirl atomizer model, which is also known as the Linearized Instability Sheet Atomization (LISA) model [8], is used to specify the fuel atomization process. The LISA model assumes that the transition from internal injector flow to fully-developed spray is divided into three steps: film formation, sheet breakup, and atomization. The geometry of the atomizer and the location of the spray injection are also specified in the atomizer model.

In the droplet breakup process, the primary breakup is not treated in this study. Therefore, only the secondary breakup process of initially injected liquid fuel is considered. The Kelvin-Helmholtz breakup model [9] or the Wave model is chosen, since it is more suitable for high Weber-number flows as in the present study. The model considers that the breakup of the droplets to be induced by the relative velocity between the gas and liquid phases. It assumes that the time of breakup and the resulting droplet size are related to the fastest-growing Kelvin-Helmholtz instability, derived from the jet stability analysis. The wavelength and growth rate of this instability are implemented to predict the details of the newly-formed droplets.

The radius of the newly-formed droplets is considered to be proportional to the wavelength of the fastest-growing unstable surface wave on the parent droplet:

$$r = B_0 \Lambda \quad (8)$$

where B_0 is a model constant, which is set to 0.61 [9] and Λ is the wavelength of the fastest-growing wave. The rate of change of droplet radius in the parent parcel is given by

$$\frac{da}{dt} = -\frac{a-r}{\tau}, r \leq a \quad (9)$$

where a is the parent drop or jet radius and τ is the breakup time, which can be expressed as:

$$\tau = \frac{3.726 B_1 a}{\Lambda \Omega} \quad (10)$$

where B_1 is the breakup time constant, Ω is the maximum wave growth rate on the drop surface for the corresponding wavelength Λ . For the stripping breakup process, when the droplets are exposed to a violent disturbance, $B_1 = \sqrt{3}$ has been found to be satisfactory [9]. In the present investigation, the same value for the breakup time constant is considered.

In the wave model, mass is accumulated from the parent drop at a rate shown by the expression for the breakup time τ , until the shed mass is equal to 5% of the initial parcel mass. At this time, a new parcel is created with the newly formed droplets and their radius is calculated using Eqn 8.

Additionally, in the present study, the Dynamic Drag Model (DDM) is specified to include the effect of drop oscillation and distortion on the drop drag coefficient using the following relation [10]:

$$C_D = C_{D,sphere}(1 + 2.632y) \quad (11)$$

where $C_{D,sphere}$ is the drag coefficient of the spherical droplet. The above equation indicates that the drag coefficient of a distorted drop should lie between that of a rigid sphere and that of a disk, whose drag coefficient at high Reynolds numbers is about 3.6 times higher than that of a sphere.

For collision and coalescence modeling, the stochastic method of O'Rourke [11] has been used in the code.

2.4 Turbulence Dispersion Modeling

The dispersion of liquid particles due to turbulence in the gas phase is predicted by using the stochastic tracking or Discrete Random Walk Model (DRWM). The model includes the effect of instantaneous turbulent velocity fluctuations on the particle trajectories through the use of stochastic methods.

The stochastic tracking approach predicts the turbulent dispersion of particles by integrating the trajectory equations for individual particles, using the instantaneous fluid velocity, $\bar{u} + u'(t)$, along the particle path during the integration. By computing the trajectory for a sufficient number of representative particles, the random effects of turbulence on the particle dispersion may be accounted for.

2.5 Combustion Modeling

In the present reacting case, the mixture-fraction/PDF modeling approach is used to model the non-premixed turbulent combustion by solving a transport equation for a single conserved scalar, called the mixture fraction. Multiple chemical species, including radicals and intermediate species, can be incorporated in the problem definition and their concentrations are derived from the predicted mixture fraction by using the assumption of equilibrium chemistry. The properties of the species are accessed through a chemical database. This approach is effective because atomic elements are conserved in chemical reactions. As a result, the mixture fraction is a scalar quantity and its governing transport equation does not consist a source term. In the present case, using this model, combustion is simplified to a mixing problem, and the complications associated with closing non-linear mean reaction rates are avoided.

The interactions between turbulence and chemistry are modeled by using the Beta PDF(β -PDF) closure model. The shape of the PDF, $p(f)$, produced by the β function depends on the mean mixture fraction (\bar{f}), and its variance ($\overline{f'^2}$). The Fluent@code

predicts \bar{f} and $\overline{f'^2}$ at each point in the flow field, thereby computing the assumed PDF shape $p(f)$, which is used as a weighting function to determine the mean values of species mass fractions, density, and temperature.

$C_{12}H_{23}$ is considered as a liquid fuel to approximate the experimental Jet-A fuel. The equilibrium mixture consists of 20 chemical species. A non-adiabatic combustion system is considered when the PDF look-up tables are constructed.

3 Experimental Setup, Boundary Conditions, Grid, and Numerical Approach

3.1 Experimental Setup

The LDI combustor experimental setup is designed by the NASA Glen Research Center. The experimental data for the single-element LDI geometry is provided by Cai et. al [4]. The single-element fuel injector module is illustrated in Figure 2. It comprises a 60°, six helicoidal swirled-vaned inlet, followed by a short converging-diverging venturi that ends at the dump plane of a square combustion chamber. The outer and inner diameters of the swirler are 22.5 mm and 8.8 mm respectively. The calculated swirl number is 1.0 [4]. Both converging and diverging angle of the venturi are 45°. The design of the converging-diverging venturi is made such that it can lower the chances of the return of the spray droplet from downstream and prevent flame flashback and auto ignition inside the swirler [4]. The fuel injector is inserted through the center of the swirler and the fuel tip is placed at the throat of the venturi. The fuel nozzle is a 90°, hollow cone, pressure swirl atomizer. The diameter of the orifice is 0.0005 m.

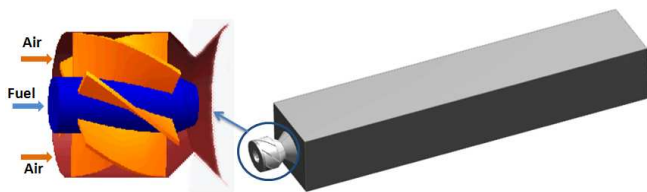


Figure 2. The single-element LDI combustor geometry with the air swirler-fuel injector configuration being zoomed in

3.2 Initial and Boundary Conditions

For both non-reacting and reacting case, air at stagnation temperature $T_0 = 294.28$ K and 1 atmosphere pressure enters with a flow velocity of $U_0 = 20.14$ m/s normal to the inlet face. Inlet air density is 1.19 kg/m³. Turbulence specification method is intensity and length scale with 10% turbulent intensity and one

tenth of inlet diameter length scale. The fuel is injected at 0.415 g/s, which in combination with the air mass flow rate gives an equivalence ratio of 0.75 for the reacting case. The fuel atomizer is operated at a pressure of 110 kPa.

3.3 Grid and Numerical Approach

The computational work presented here is carried out for a single-element LDI combustor module. An implicit finite-volume scheme with second order accuracy in space and time is employed. Computation is performed for the entire geometry including the flow development section for the incoming air, six swirling passages for the injector module, convergent-divergent venturi, and the rectangular flame tube. The grid has been refined a few times in order to investigate the effects of grid density on the flow field. The grid consists of hexahedron and tetrahedron elements. The final refined grid for the single-element model, as shown in Figure 3, has 2,374,805 elements. The grid is clustered normal to the walls to resolve the large gradients through the boundary layer.

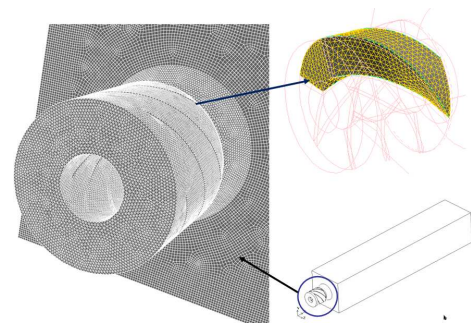


Figure 3. Grid distribution for the single-element configuration

The pressure-based solver is used with the coupled pressure-velocity coupling scheme. The third-order MUSCL discretization method is specified to solve the momentum equations and the second-order upwind scheme is applied to solve the other equations. A higher-order convective discretization scheme is suitable for the present problems involving highly turbulent flows inside the swirlers and complex flows at the combustion chamber inlet. Furthermore, the flow is not aligned with the grid due to the presence of tetrahedral and hexahedral elements. Therefore, a higher-order scheme is expected to yield greater accuracy and decrease the possibility of numerical discretization error.

The computation is carried out until the solution becomes statistically stable. In the URANS calculations for the non-reacting case, at first, a steady flow state Realizable $\kappa - \epsilon$ model is used to create a realistic initial flow field for the unsteady computations. Once the flow field is reasonably converged, unsteady

calculation is enabled. The unsteady $\kappa - \epsilon$ calculation is continued until the flow becomes statistically stable. Thereafter, the solution is restarted using the RSTM. When the flow is fully developed and statistically stable, time-averages are calculated by sampling at a specified frequency to obtain both mean and root mean square values. Likewise, the calculation is continued until statistically stable data is obtained. The duration of the computation is determined beforehand by estimating the mean flow residence time in the solution domain. The standard measure for the convergence of the iterations is the residuals of the equations being solved. In the present case, it is observed that when the residuals of the continuity, momentum, and Reynolds stresses equations drop by more than five orders of magnitude, there is no appreciable change in the solution. Thus at that stage, the case is considered as converged. The balance of mass flux into and out of the computational domain is also monitored. When the convergence is reached, the mass imbalance is found to have a very small fraction of the total flux (of the order of 10^{-8}) through the system. For the URANS calculation, the physical time-step is $1.0E-06$ (s) and the CFL number for the pseudo time iteration is less than 1.

For the reacting case, a steady state RANS simulation is performed for the gas-phase calculations. The liquid-phase is modeled by using the Discrete Phase Model (DPM) with the unsteady particle tracking approach. The Realizable $\kappa - \epsilon$ model is used to specify the turbulence. For the liquid spray calculations, models for atomization, droplet breakup, droplet coalescence and collision, droplet drag, and turbulent dispersion are incorporated in the DPM. In addition, the mixture-fraction/PDF modeling approach is used to model turbulent combustion inside the LDI combustor. Simulation is conducted until the residuals of the continuity, momentum, and energy equations drop by more than five orders of magnitude, and no significant changes are found in the solution.

4 Results and Discussion

In this section, the computed results for non-reacting and reacting flow field of the single-element LDI combustor are separately reported. The results between two cases are compared. Furthermore, the computed data are compared with the measurement data [4].

4.1 Non-reacting Flow Field

Figures 4 and 5 are the axial mean velocity contours in the X-Y plane and the iso-surface of zero axial mean velocity respectively. The iso-surface of the zero axial mean velocity is also known as the vortex breakdown bubble (VBB). The figures indicate the presence of a very large recirculation zone in the central core region, which extends upstream up to the injector tip. At low swirl numbers, there may be a significant radial pressure gra-

dient at any axial position caused by the centrifugal effects, but the axial pressure gradient is relatively low. Nevertheless, when increasing the swirl, a strong coupling develops between axial and tangential velocity components and the axial (adverse) pressure gradient increases. A point is reached, when the adverse pressure gradient along the jet axis cannot be further overcome by the kinetic energy of the fluid particles flowing in the axial direction, and a recirculation flow is set up in the central portion of the jet. The formation of the recirculation zone, a form of vortex breakdown, acts as an aerodynamic blockage or a three dimensional bluff body which stabilizes flames. This is essential to provide sufficient residence time, temperature, and turbulence for a complete combustion of the fuel. In addition to the major recirculation zone at the center, there are two other regions in which the flow is reversed, one is located in the diverging section of the venturi and the other one is found in the corner of the upstream wall of the combustion chamber. The presence and the interaction of these vortical structures make the mean flow unsteady in the frontal region. The high fluctuating velocity, as shown later, further demonstrates the existence of the large degree of unsteadiness in this region.

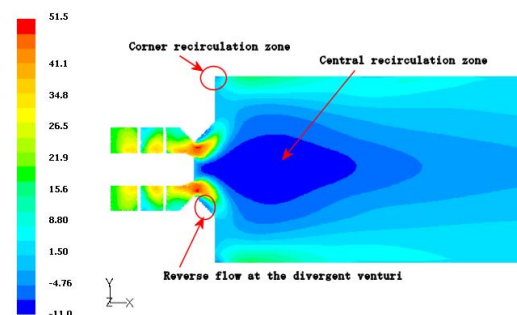


Figure 4. Axial mean velocity distributions (in m/s)



Figure 5. VBB of the single-element LDI combustor (side view)

The axial mean normal stress distribution at the centerline is compared to the measurements at various axial locations in Figure 6. The axial normal stresses have the highest value at the swirler exit owing to the high level of turbulence resulting from the high degree of swirling flow. After this, the axial normal stress decays rapidly and then becomes almost constant within the recirculation zone. Although it levels off, it still decays as the flow moves to the downstream.

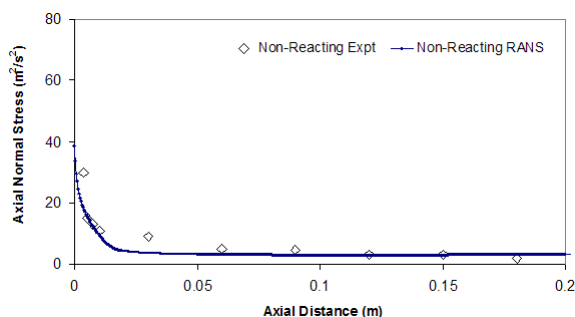


Figure 6. Computed centerline axial mean normal stress vs. experimental data

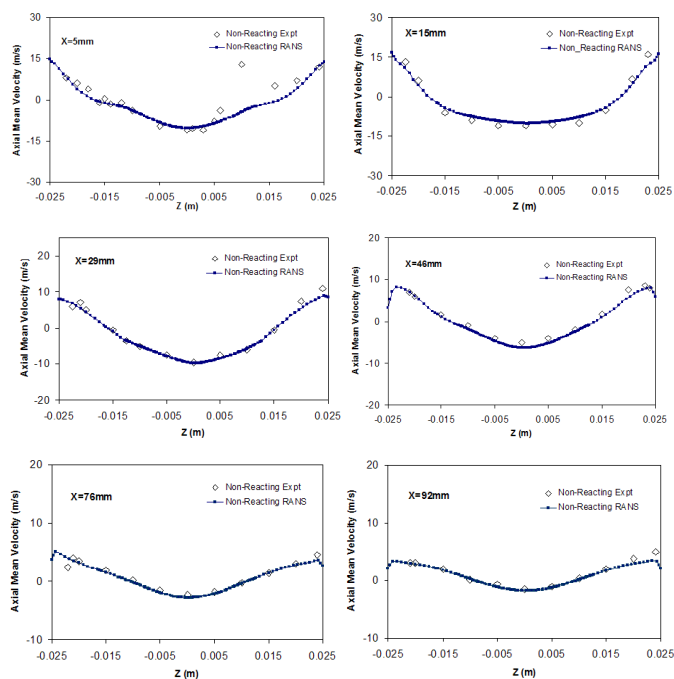


Figure 7. Computed non-reacting axial mean velocity at various axial locations compared with measurements

Figure 7 compares the computed axial mean velocity distribution along the radial direction with the measured data for different axial locations. At 5mm downstream, both measurements and computed URANS data indicate the presence of an axial mean velocity peak away from the centerline and a reverse flow region in the central part. Nevertheless, the computed results exhibit symmetrical profiles unlike the measured data. The discrepancy at this location may be due to various reasons. Apart from the computational issues such as grid resolution, there was also difficulty in obtaining accurate experimental data at this location as stated in the literature [4]. Nevertheless, at all other locations, the computed data for the mean axial velocity profiles have a good agreement with the measurements, which do show almost symmetry over there. Both measured and computed data exhibit axial velocity peaks near the wall of the combustion chamber when the flow hits the wall. As the flow moves downstream, the axial mean velocity peak, initially observed away from the centerline at the location $x=5\text{mm}$, flattens out due to expansion of the recirculation zone in the central region. On the other hand, further downstream, the magnitude of the axial velocity peaks close to the chamber wall also decreases. At $x=92\text{mm}$, the axial velocity profile shows an almost flat velocity distribution. However, as discussed later, the axial velocity profiles for the reacting case is quite different from the non-reacting case.

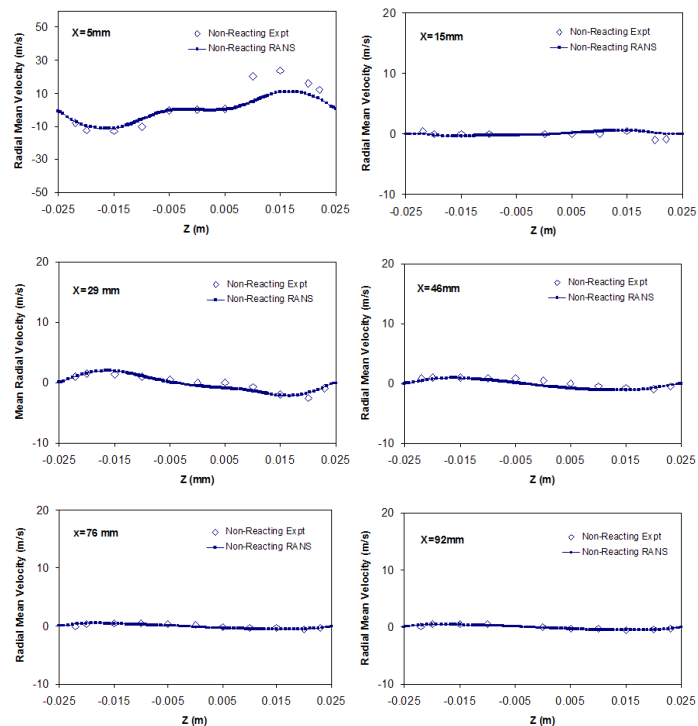


Figure 8. Computed non-reacting radial mean velocity at various axial locations compared with measurements

Comparisons of the radial mean velocity for various axial stations are shown in Figure 8. The radial velocity is high as the flow enters the combustion chamber. Therefore, at 5 mm downstream, the radial velocity has higher magnitude than at other axial locations. The profile indicates a quick expansion of the flow in the radial direction. Nevertheless, some discrepancies with the measurements are observed at this station along the positive radial direction. Unfortunately, it is the same location where measurements are uncertain. At 15 mm downstream, the radial velocity is almost zero. Further downstream, at 29mm and 46mm, the radial velocities change direction owing to the shrinkage of the recirculation zone. The radial mean velocity profiles are relatively flat at 76mm and 92mm downstream of the combustion chamber inlet.

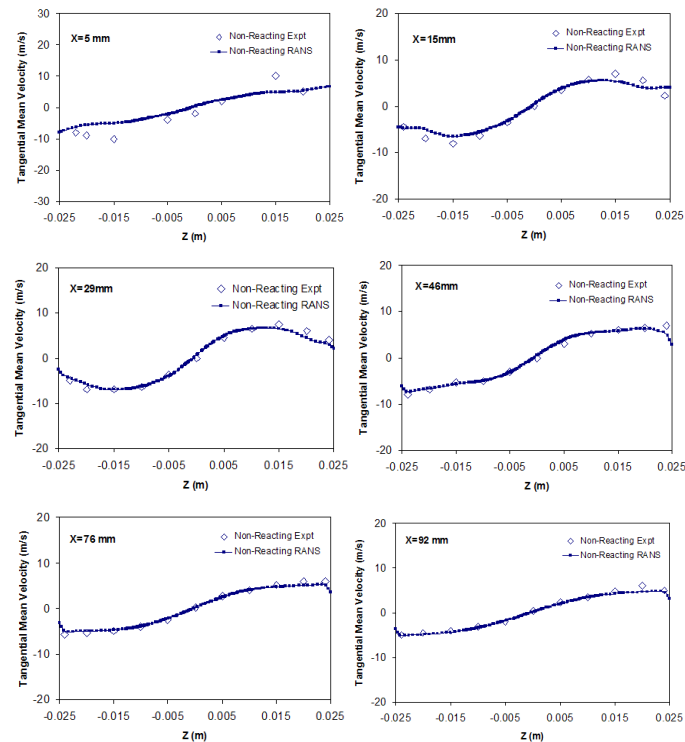


Figure 9. Computed non-reacting tangential mean velocity at various axial locations compared with measurements

Figure 9 compares the computed tangential mean velocity profiles to the measurements at different axial locations. This velocity component, which essentially represents the swirl of the flow, is important since the combustor is designed for creating high swirling flows to enhance the mixing of fuel and oxidizer. At the initial stations (at 15mm and 29mm downstream), the tangential velocity profiles indicate the formation of a com-

bined solid and free vortex structure. Further downstream, peak swirling velocity moves outward and a solid vortex profile is established. Furthermore, it is observed that unlike the radial velocities, the tangential velocities are much higher even in the downstream.

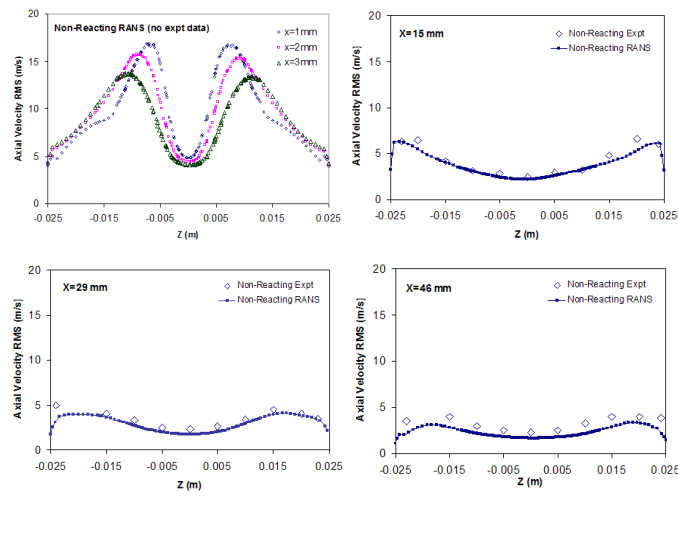


Figure 10. Computed non-reacting axial RMS velocity at various axial locations

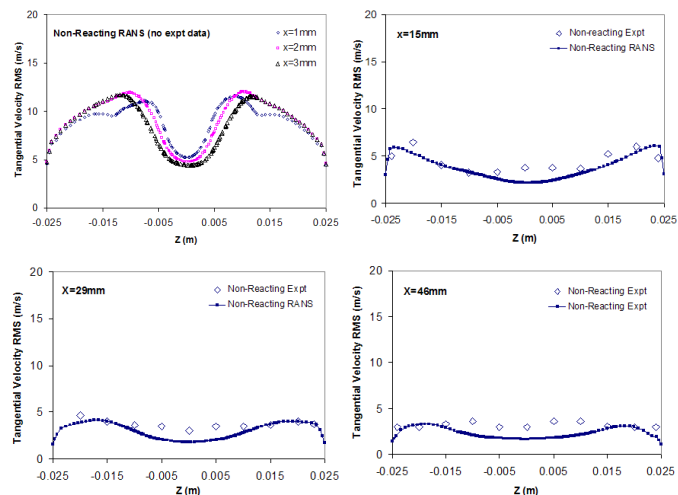


Figure 11. Computed non-reacting tangential RMS velocity at various axial locations

Figures 10 and 11 show the components of the turbulent velocity profiles at various axial locations. The root-mean-squared

(RMS) values presented here represent the turbulent velocities. Turbulent velocities are computed at 3 additional stations very close to the combustion chamber inlet, where no experimental data are provided. The velocities in these 3 locations, namely 1mm, 2mm, and 3mm downstream of the chamber inlet, are plotted together. Figure 10 shows stronger turbulent axial velocities close to the chamber inlet. However, they decay rapidly in the downstream.

Similar behavior is observed for the turbulent tangential velocity profiles, as shown in Figure 11. At 1mm downstream, the peak axial turbulent velocity is around 17m/s, while the peak tangential turbulent velocity is 11m/s respectively. Such variations in the components of the turbulent velocity are also observed at the two other axial locations close to the chamber inlet. The different turbulent velocity profiles among three components found in these axial locations indicate the non-isotropic Reynolds stress distribution induced by the high swirling flow.

Overall, the numerical modeling of the non-reacting flow field in the single-element LDI combustor using the URANS method coupled with the $\kappa - \epsilon$ and RSTM turbulence models exhibits good agreement with the measurements. The accuracy of the current URANS results are comparable with the numerical results reported in the literature [12] using the LES scheme.

4.2 Reacting Flow Field

Figure 12 shows the centerline axial velocity along the length of the combustor. The central recirculation region for the reacting case is significantly stronger as compared to that of the non-reacting case, due to the effect of heat release resulting from combustion. Nevertheless, the length of the reverse flow region in the latter case is twice as much as the length for the former case. Furthermore, the figure indicates that flow acceleration from 1 m/s for the non-reacting case to 15 m/s for the reacting case in the downstream.

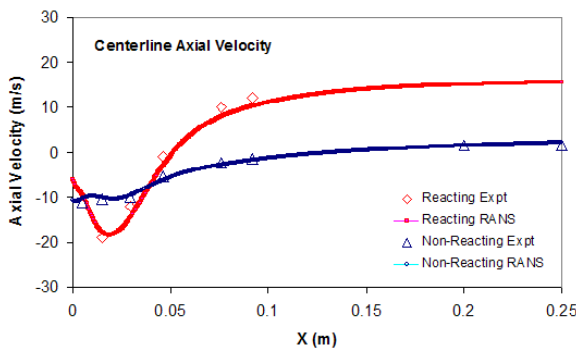


Figure 12. Computed centerline axial velocity for the non-reacting and reacting case vs. experimental data

The radial profiles for axial velocities are compared to the measurements [4] at various axial locations in Figure 13. At the first measurement station, the RANS data predict a strong recirculation in the central portion with almost symmetric peaks on either sides. On the other hand, the measurement data do not exhibit any reverse flow and the velocity magnitude is relatively higher. However, in the experimental study [4], the authors mentioned about the difficulty in sorting the seeding particles from high momentum spray particles at this location. This may be the reason why the positive axial velocities are measured in spite of a reverse flow zone. Further downstream, the comparison between RANS and the measurements are quite reasonable. It can be observed that at 15mm and 29 mm downstream, where intense reaction takes place, the expansion of the hot reacting gas-phase leads to narrow reverse flow zones with higher reverse velocities as compared to the non-reacting flow (as shown earlier in Figure 7). At 46 mm downstream, the recirculation zone almost disappears due to high axial momentum. Further downstream, at 76mm and 92mm, although the velocity profiles show a relatively flat velocity distribution, they still possess higher magnitude as compared to that of the non-reacting case at these locations.

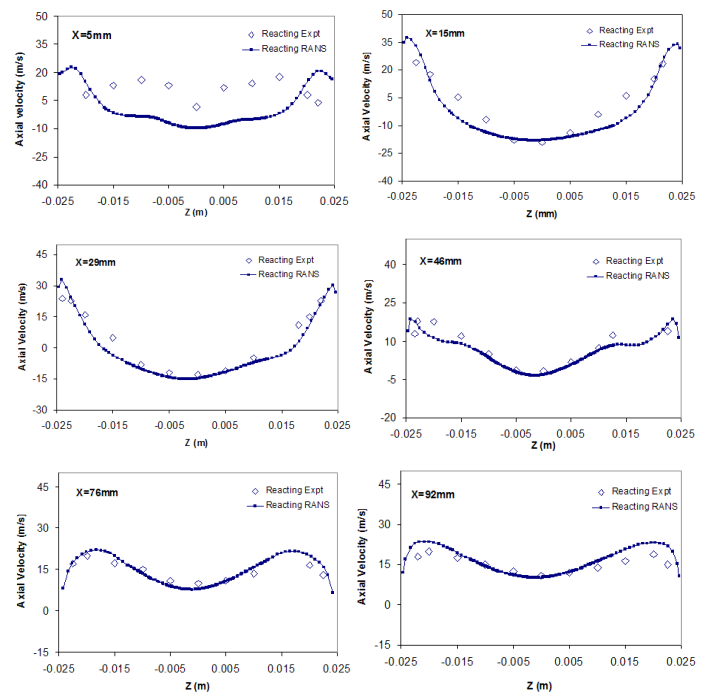


Figure 13. Computed reacting axial velocity at various axial locations compared with measurements

Figure 14 exhibits the tangential velocity distribution. The reacting gas-phase swirl velocity has higher magnitude com-

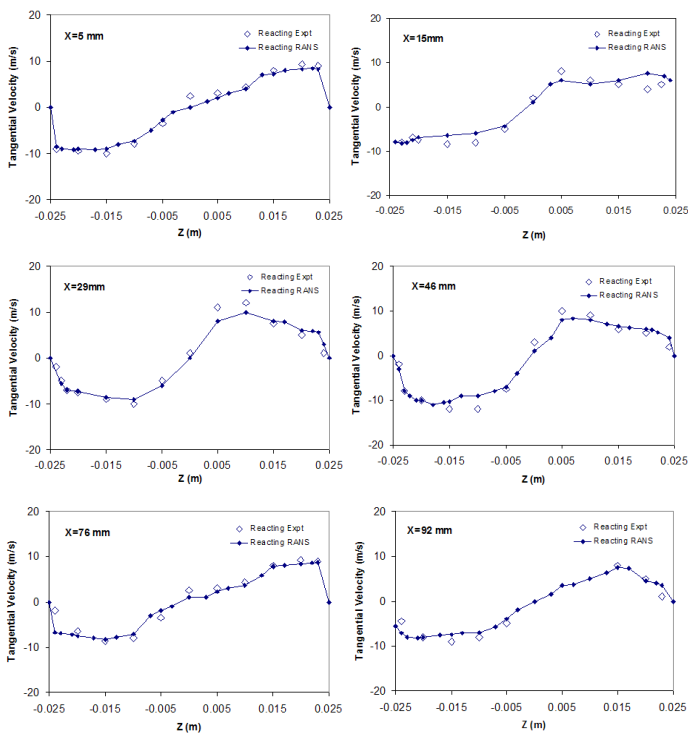


Figure 14. Computed reacting tangential velocity at various axial locations compared with measurements

pared with the non-reacting case. This could be due to the presence of the low density gas phase at high temperature. Unlike in the non-reacting flow, the reacting case shows that the peak velocity moves towards the center. Except at 5 mm downstream, the reacting gas-phase velocity profiles at the other locations form a combined vortex structure. This can be attributed to the short recirculation zone for the reacting case and as the flow goes past the recirculation zone, the redistribution of the flow field results in the combined vortex profile. The computed data for the tangential velocities shows a good agreement with the measured data at all the axial locations.

Figure 15 shows the instantaneous temperature profiles in the X-Y plane at $Z=0$. The equivalence ratio computed from the inlet boundary conditions is about 0.75. The adiabatic flame temperature is approximately 2100 K. The mean temperature at the exit plane is between 1750 K and 1850 K. The experiment does not provide the temperature profiles. However, the computed results for the temperature plots are compared with the numerical predictions using the laminar chemistry model in the National Combustion Code (NCC) [13]. The temperature profiles obtained from the present simulation show good agreement with literature. Figures 16(a) and 16(b) show the temperature profiles at 40mm downstream and at the chamber exit respectively. Figure 16(a) indicates that the higher temperature regions exist in

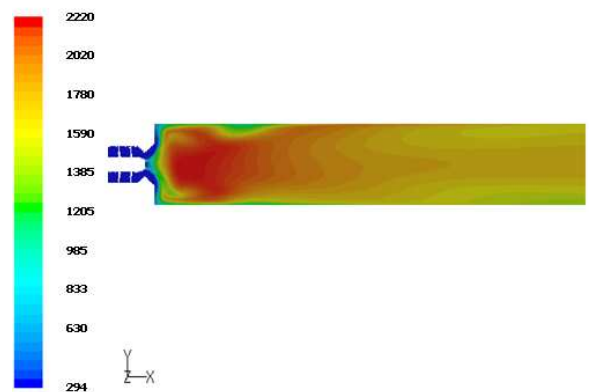
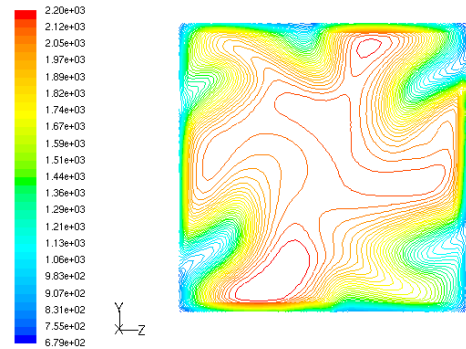
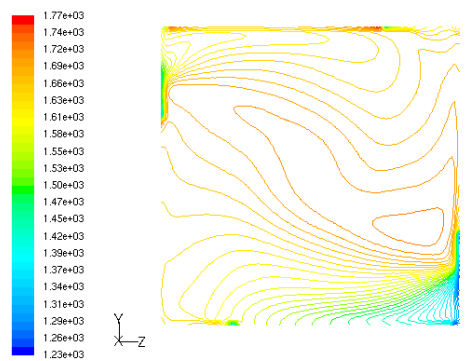


Figure 15. Computed temperature profiles (in Kelvin) on the X-Y plane at $Z=0$



(a) At 40 mm downstream



(b) At the combustion chamber exit

Figure 16. Computed temperature profiles (in Kelvin) inside the combustor

the central portion, which spread and mix with the low temperature regions close to the wall. The high swirling flow inside the combustor also plays an important role in the mixing process. Nevertheless, towards the exit, as shown in Figure 16(b), an almost uniform temperature profile is observed, and the initial

higher temperature regions have merged with the lower temperature regions, thereby forming a moderate temperature zone at the exit.

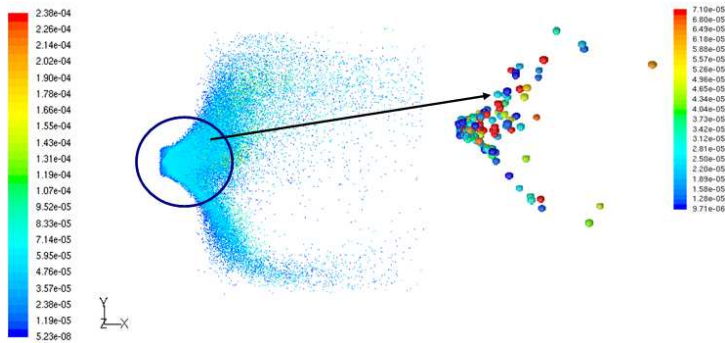


Figure 17. Particle tracks for the spray injection (particle diameter shown in meters)

Figure 17 exhibits the trajectories of the droplets in the spray injection, which allow to review the locations of the droplets. The trajectories terminate when the liquid fuel is completely vaporized. 15,000 droplet parcels are introduced into the domain at every time step by implementing the LISA atomization model [8]. In essence, each of these discrete droplet streams has its own set of initial conditions. From the figure, it can be observed that the maximum diameter of the droplets is about $2e^{-04}$ m or 0.2mm. Nevertheless, the diameter of most of the droplets in the spray domain is between $20\mu\text{m}$ and $70\mu\text{m}$, which is consistent with the Sauter Mean Diameter (D_{32}) of the droplets obtained from the measurement. Furthermore, it is found that almost all the droplets vanish at 25mm downstream due to evaporation, and there is a significant reduction in liquid volumetric fraction after 15mm downstream. The figure also illustrates droplet breakup process and coalescence among the droplets. Coalescence of initially smaller droplets results in bigger diameter drops in the downstream, as shown in the zoomed-in view in Figure 17. Around 20 particle streams are shown in this view to demonstrate the droplet breakup and coalescence phenomena. It is further observed that each particle stream is randomly oriented until the particle evaporates. Therefore, the smaller droplets are expected to be following the paths of the gas-phase flow field induced by the swirling flow. It is also expected that the possible presence of the spiralling precessing vortex cores in the neighborhood of the injector might influence particle dispersion.

Nevertheless, in order to validate the spray model, it is important to investigate the size, position, and statistics of the droplets in more details and compare them with the measurements.

5 Conclusions

Numerical simulation is performed for the non-reacting and reacting flow field associated with a single-element LDI combustor. The simulation is conducted for the entire geometry, encompassing six helicoidal air flow passages and the square combustor chamber. The results are compared with the measurements. The solution for the non-reacting flow captures the essential aerodynamic flow characteristics of the LDI combustor, such as the complex swirling flow structures inside the swirlers and in the vicinity of the combustion chamber inlet, the large central recirculation zone originating from the tip of the fuel injector, and the reverse flow regions at the corners of the chamber wall and on the wall of the divergent venturi, with reasonable accuracy. Furthermore, the calculated mean and turbulent velocity components at various axial locations within the combustor exhibit good quantitative agreements with the measurement data.

A spray model is introduced to simulate the reacting flow field. The reaction of the spray greatly influences the gas-phase velocity distribution. The high axial momentum induced by combustion and momentum transfer between liquid and gas phase cause the decrease of the recirculation region in the reacting case. In addition, the heat release due to combustion leads to an expansion of the gas-phase, which results in higher velocities as compared to the non-reacting case. The computed gas-phase velocity profiles are consistent with the experimental data. The temperature profiles indicate that the swirling flow influences the higher temperature regions to spread and mix with the low temperature regions, and towards the exit a near uniform temperature profile is observed. The Kelvin-Helmholtz breakup model in combination with the Dynamic Drag Model is implemented in the RANS code to characterize the droplet breakup process. Turbulent dispersion effect is also included in the spray model. The solution indicates that the evaporation of almost all the droplets occurs within a few millimeters inside the combustion chamber. The computed droplet size is reasonable compared with the measurements. The computed data shows the influence of the swirling flow on the droplet breakup and coalescence process. The temperature plots and the spray behavior indicate a rapid and homogeneous mixing occurring inside the LDI combustor, which might result in low emissions of pollutants.

The present study reveals that the commercial RANS code with the realizable $\kappa-\epsilon$ and RSTM turbulence models can effectively predict the complex flow field behavior of the LDI combustor for both non-reacting and reacting flows. However, a detailed validation of the current spray model is required, which will be obtained in the future by comparing with the experimental measurements of the locations, size, and statistics of liquid droplets.

REFERENCES

- [1] Dewanji, D., Rao, A.G., and van Buijtenen, J.P., "Conceptual Study of Future Aero-engine Concepts," *International Jour-*

- nal of Turbo and Jet Engines*, Vol. 26, No. 4, 2009, pp. 263-276.
- [2] Tacina, R., Lee, P., and Wey, C., "A Lean-Direct-Injection Combustor Using a 9 Point Swirl-Venturi Fuel Injector," *IS-ABE*, ISABE-2005-1106, 2005.
- [3] Heath, M.C., Hicks, R.Y., Anderson, R.C., and Locke, R.J., "Optical Characterization of a Multipoint Lean Direct Injector for Gas Turbine Combustors: Velocity and Fuel Drop Size Measurements," *Proceedings of ASME Turbo Expo 2010: Power for Land, Sea and Air GT2010*, GT2010-22960, June, 2010, Glasgow.
- [4] Cai, J., Jeng, S.-M., and Tacina, R., "The Structure of a Swirl-Stabilized Reacting Spray Issued from an Axial Swirler," *43rd AIAA Aerospace Sciences Meeting and Exhibit*, AIAA Paper 2005-1424, 2005, Reno, NV.
- [5] Trinh, H. P., and Chen, C. P., "Modeling of Turbulence Effects on Liquid Jet Atomization & Breakup," *43rd AIAA Aerospace Sciences Meeting and Exhibit*, AIAA-2005-0154, January, 2005, Reno, NV.
- [6] O'Rourke, P. J., and Amsden, A. A., "The TAB Method for Numerical Calculation of Spray Droplet Breakup," *SAE Technical Paper* 872089, 1987.
- [7] Williams, F.A., *Combustion Theory*, 2nd Edition, Addison-Wesley Publishing Co., Reading, MA, 1985, pp. 250.
- [8] Schmidt, D. P., Nouar, I., Senecal, P. K., Rutland, C. J., Martin, J.K., and Reitz, R. D., "Pressure-Swirl Atomization in the Near Field," *SAE*, SAE Paper 01-0496, 1999.
- [9] Reitz, R. D., "Mechanisms of Atomization Processes in High-Pressure Vaporizing Sprays," *Atomization and Spray Technology*, Vol. 3, 1987, pp. 309-337.
- [10] Liu, A. B., Mather, D., and Reitz, R. D., "Modeling the Effects of Drop Drag and Breakup on Fuel Sprays," *SAE Paper* 930072, 1993.
- [11] O'Rourke, P.J., "Collective Drop Effects on Vaporizing Liquid Sprays," PhD Thesis, Princeton University, 1981, New Jersey.
- [12] Davoudzadeh, F., Liu, N.-S. and Moder, J. P., "Investigation of Swirling Air Flows Generated by Axial Swirler in a Flame Tube," *Proceedings of GT2006 ASME Turbo Expo 2006: Power for Land, Sea and Air* May 8-11, 2006, Barcelona, Spain.
- [13] Wey, T., and Liu, N.-S., "Assessment of Turbulence-Chemistry Interaction Models in the National Combustion Code (NCC)-Part I," *48th AIAA Aerospace Sciences Meeting*, AIAA 2010-1170, January, 2010, Orlando.